Applied Thermal Engineering 182 (2021) 116063

Contents lists available at ScienceDirect

Applied Thermal Engineering

journal homepage: www.elsevier.com/locate/apthermeng

Analysis of the membrane effects on the energy efficiency of water desalination in a direct contact membrane distillation (DCMD) system with heat recovery

Kleber Marques Lisboa [a,*], Diego Busson de Moraes [b], Carolina Palma Naveira-Cotta [b], Renato Machado Cotta [b,c]

[a] Laboratory of Thermal Sciences (LATERMO), Department of Mechanical Engineering – TEM/PGMEC, Universidade Federal Fluminense – UFF, Niterói, RJ, Brazil
[b] Laboratory of Nano & Microfluidics and Microsystems (LabMEMS), Mechanical Eng. Dept., POLI & COPPE, Universidade Federal do Rio de Janeiro, UFRJ, Brazil
[c] General Directorate of Nuclear and Technological Development, DGDNTM, Brazilian Navy, Ministry of Defense, RJ, Brazil

ARTICLE INFO

Keywords:
Direct contact membrane distillation
Desalination
Waste heat recovery
Transport in porous media

ABSTRACT

A theoretical analysis of the energy efficiency of a direct contact membrane distillation (DCMD) module with external heat recovery intended for desalination applications is carried out. A porous media model is proposed and validated against previously reported numerical and experimental results. A 2^n planning scheme is employed to determine the most decisive membrane properties for maximizing the energy efficiency of the desalination system. The interaction between membrane parameters are found to be weak, allowing for the selection of manufacturing processes for emphasis in certain parameters. The porosity is shown to be a dominant factor, responsible for at least 40% of the variation of the energy efficiency metric, while the relative importance of other parameters is dependent on the heat recovery system effectiveness. An optimum membrane thickness is identified and observed to become smaller for better heat recovery systems, improving the energy efficiency of the process. The results obtained offer guidance to future membrane development efforts as to what should be emphasized to maximize the amount of distilled water produced for a given heat input. In particular, harnessing the interaction between the membranes parameters and the heat recovery system is essential to leverage the energy efficiency of the desalination system.

1. Introduction

Water is increasingly scarce in several locations around the world, pushing for the development of effective ways to obtain potable water from brackish and seawater through desalination [1]. Membrane-based desalination technologies rely on a physical barrier that allow either ions or water molecules to migrate from the salt water compartment and to be collected on the opposite side of the membrane. The most prominent methods of membrane-based desalination are reverse osmosis (RO) [2], forward osmosis (FO) [3], and electrodialysis (ED) [4]. On the other hand, thermal-based desalination techniques use heat to vaporize water, thereby separating the water from the non-volatile components initially dissolved in it. Nuclear reactors, for instance, could offer an interesting cogeneration alternative associated with the use of the substantial waste heat for thermal-based desalination [5], in place of burning fossil fuels. There are two main thermal-based desalination methods, namely multi-stage flash (MSF) [6] and multi-effect distillation (MED) [7]. The former is currently the most used thermal method for desalination, but MED is gradually surpassing due to its superior energy efficiency [8].

With the intent of combining desirable characteristics of both membrane- and thermal-based desalination techniques, membrane distillation (MD) was proposed. The membrane distillation is driven by a partial pressure difference that forms across a hydrophobic membrane sandwiched between a hot feed and a compartment that may contain distilled water, air or vacuum, depending on the specific technique being used. This method is known for the capacity of working with high salinity brines and mild pressures without compromising the water flux, while producing essentially distilled water, in deep contrast with reverse osmosis [9,10]. However, for salinities above 10 wt%, a significant performance degradation may occur in MD [11]. In addition, MD can be

* Corresponding author at: Laboratory of Thermal Sciences (LATERMO), Department of Mechanical Engineering – TEM/PGMEC, Universidade Federal Fluminense – UFF, Niterói, RJ, Brazil.
E-mail address: kmlisboa@id.uff.br (K. Marques Lisboa).

https://doi.org/10.1016/j.applthermaleng.2020.116063
Received 4 May 2020; Received in revised form 8 September 2020; Accepted 11 September 2020
Available online 17 September 2020
1359-4311/

Nomenclature

a	Specific surface area
$c_{p,\gamma}$	Specific heat at constant pressure of phaseγ
$d_{h,\gamma}$	Hydraulic diameter of phaseγ
d_p	Mean pore diameter
GOR	Gain-output ratio
h	Heat transfer coefficient
h_{fg}	Latent heat of vaporization
$j_{w,l}$	Local distilled water mass flux based on the internal area of the hollow fiber
$\bar{j}_{w,l}$	Average distilled water mass flux based on the internal area of the hollow fiber
k_m	Effective thermal conductivity of the membrane
k_p	Thermal conductivity of the membrane polymer
k_v	Thermal conductivity of water vapor
k_γ	Thermal conductivity of phaseγ
$\mathbf{K}$	Permeability tensor
L	Effective length of the vessel
m	Indicator of lumen and shell sides
$MGOR$	Mechanical gain-output ratio
M_w	Molecular weight of water
$\mathbf{n}$	Outward drawn unit vector
N_{fbr}	Number of hollow fiber membranes
Nu	Nusselt number
$N_{w,l}$	Distilled water molar flux based on the internal area of the hollow fiber
p	Partial pressure
P	Pressure within the membrane pores
Pe	Péclet number
$p_{f,\gamma}$	Intrinsic phase average pressure
Pr	Prandtl number
$p_{v,\gamma}$	Vapor pressure at the interface between the membrane and the streamγ
$\dot{q}$	Heat transfer
Q	Volume flow rate
r	Radial coordinate
R	Universal gas constant
Re	Reynolds number
r_l	Internal radius of the hollow fiber membrane
r_s	External radius of the hollow fiber membrane
r_v	Internal radius of the vessel
T_m	Average temperature along the membrane
$T_{m,\gamma}$	Temperature at the interface between the membrane and phaseγ
T_γ	Temperature of phaseγ
$\mathbf{u}$	Phase average velocity
u	Axial component of the phase average velocity
$\dot{W}_p$	Total pumping power
$x_{salt,\gamma}$	Molar fraction of salt in the streamγ
z	Axial coordinate

Greek letters

ε_γ	Porosity of phaseγ
ε_m	Porosity of the membrane
μ	Dynamic viscosity of water
ρ	Density of water
τ	Tortuosity of the membrane

Subscripts and superscripts

a	Air
c	Characteristic value
e	Inlet condition
w	Water
γ	Indicator of the lumen side when l and of the shell side when equal to$s$
$*$	Dimensionless quantity

applied to small-scale operations with low-grade waste heat sources more efficiently than other thermal-based methods such as MED and MSF [12]. Amongst the different MD types, the direct contact membrane distillation (DCMD) is regarded as the easiest to build and operate [10,13]. In DCMD, the water vapor that migrated from the feed side is condensed at the interface between the membrane and a distilled water stream, thus dropping the need for external condensers and limiting the cost of the desalination equipment in comparison with other MD technologies [13].

Several drawbacks have prevented the widespread commercial usage of MD for mid and large scale water desalination. The major disadvantage of membrane distillation might be the large amount of thermal energy needed to desalinate a given mass of water. Thermal-based desalination methods are inherently more energy demanding than RO or ED due to the need to vaporize water [12]. The enthalpy of vaporization of water is around 2400 kJ/kg [14], whereas the Gibbs free energy of separation for seawater, which governs the energy usage in either RO or ED, amounts to 2.7 kJ/kg [15]. This difference can be significantly reduced with the use of latent heat recovery in thermal desalination processes and by taking into account the lower exergy content of heat in comparison with the work used in RO and ED. Nevertheless, even in comparison with other thermal-based techniques such as MSF and MED, the energy consumption of medium- to large-size MD facilities is still significant [12]. This fact can be majorly attributed to the presence of the membrane and the losses exacted by its mass transport resistance and parasitic heat conduction.

Commercial membranes are either manufactured with stretching, in the case of semi-crystalline polymers such as polyethylene (PE) [16] and polytetrafluoroethylene (PTFE) [17], or phase inversion, in the case of soluble polymers such as polypropylene (PP) [18] and polyvinylidene fluoride (PVDF) [19]. However, these commercial membranes are usually intended for micro- or ultrafiltration, often exhibiting undesirable features for membrane distillation. In this context, studies involving the design of dedicated membranes for MD became popular, most notably using electrospinning as the manufacturing procedure [20–22]. Membranes containing immobilized carbon nanotubes were also proposed, aiming to harness the different mass transport mechanisms it offers [23,24]. Despite its superior permeability, immobilized carbon nanotubes membranes suffer from low thermal efficiency due to their high thermal conductivity and manufacturing-related issues. In addition, several surface modification strategies were explored to enhance the hydrophobicity of the membrane. Chemical [25] and plasma [19] modifications were experimentally tested with a slight advantage for the membranes treated with plasma [26]. These techniques, along with others not reviewed here, often present limitations and are unable to deliver all desirable features of a membrane for MD applications. For instance, electrospinning is able to produce high porosity membranes, albeit it is difficult to control the pore size with this technique [26]. Therefore, knowledge of which membrane characteristics should be emphasized in future membrane manufacturing efforts is crucial.

Extensive experimental studies aiming to investigate the influence of different membrane parameters on the energy efficiency of DCMD are hindered by the limitations of the manufacturing techniques available and the costs associated with the production of several samples.

Modeling and numerical simulation are powerful tools to circumvent these difficulties. The most studied model is the one for the mass transport of water molecules through the membrane. The Dusty Gas Model (DGM) has been regarded as adequate, in spite of its limitation to isothermal transport [27–31]. The relative importance of the molecular and Knudsen transport mechanisms in MD and the influence of the Knudsen number associated with the average pore size have also been studied [32,33]. Furthermore, models for desalination modules containing hollow fiber membranes were reported in the literature [34–37]. Numerical investigations on the effects of different parameters on MD performance have also been previously reported [30,37–40]. In general, higher porosities, lower polymer thermal conductivities, and large pore sizes, though limited by the need to avoid pore wetting, are all beneficial to MD operation. As for the membrane thickness, an optimum range, dependent on the operational conditions, has been reported [11,40].

The present work aims at theoretically determining the influence of different membrane-related parameters and their interactions on the energy efficiency of a DCMD hollow fiber membrane module with an external heat exchanger for heat recovery. A porous medium heat transfer and fluid flow model for the hollow fiber bundle in conjunction with the Dusty Gas Model for the mass transport through the membrane is proposed and validated against numerical and experimental results available in the literature. A factorial analysis, employing the 2^n experimental planning procedure, is applied to investigate the effects of membrane radius, thickness, thermal conductivity, mean pore diameter, and porosity. The parameters identified as the most important are then further analyzed and design directives are offered.

2. Model and Solution Methodology

2.1. Porous medium

Direct simulation of bundles of hollow fiber membranes is a computationally intensive task, hindering optimization and system integration analyses. In order to achieve a more manageable simulation code, a porous media model for the entire module of hollow fiber membranes is proposed. Seemingly, this is the first time a porous medium model is proposed for the analysis of hollow fiber membrane distillation modules. Nevertheless, other successful applications related to oil extraction, nuclear reactors, and contaminant dispersion can be found in the open literature [42].

The vessel is considered to contain three phases, namely shell, lumen and membrane as depicted in Fig. 1.b. The membrane phase shall be modeled separately and is not included in the porous media model. Therefore, two porous medium models are associated with the shell and lumen phases as illustrated in Fig. 1.a,c. Equations for each conservation principle are associated with the porous media. The full domains for the lumen and shell sides porous medium models are represented by the cylinders of Fig. 2.a,b, respectively. These cylinders coincide with the internal shape of the vessel containing the hollow fiber bundle. The

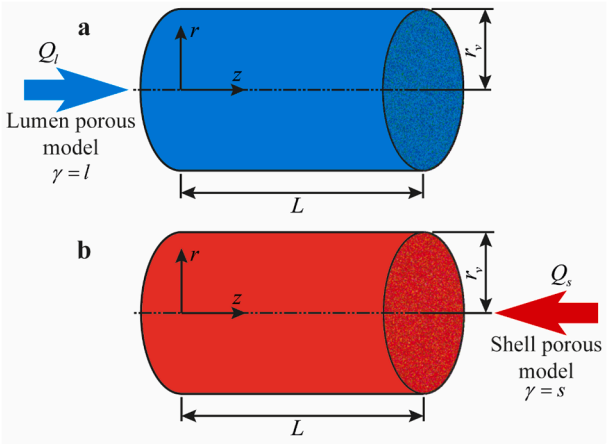

Fig. 2. Geometry of the porous media models. (a) Porous medium model for the lumen side; (b) porous medium model for the shell side. The water flows in the lumen side from left to right. Conversely, water flows in the shell side from right to left. A cylindrical coordinate system and dimensions of interest are included.

hollow fiber membranes are considered to be uniformly distributed along the cross-section of the module and with their axis parallel to the vessel axis.

The porosity is defined as the ratio between the volume of the phase and the volume of the vessel [41,42]. For the two phases we then have,

$$\varepsilon_\gamma = m + (-1)^m N_{fbr} \frac{r_\gamma^2}{r_v^2} \tag{1a}$$

with,

$$m = \begin{cases} 0, & \text{if } \gamma = l \\ 1, & \text{if } \gamma = s \end{cases} \tag{1b}$$

where γ refers to the lumen side when equal to l and to the shell side when equal to s, ε_γ is the porosity of phase γ, N_{fbr} is the number of hollow fiber membranes, r_s is the outer radius of the hollow fiber membranes, r_l is the inner radius of the hollow fiber membranes, and r_v is the radius of the vessel.

The specific surface area is the ratio of the surface area available for the transport phenomena in the phase to the volume of the vessel [42]. An appropriate expression for both porous media of Fig. 1.a,c is shown below:

$$a_\gamma = 2N_{fbr} \frac{r_\gamma}{r_v^2} \tag{2}$$

where a_γ is the specific surface area of phase γ.

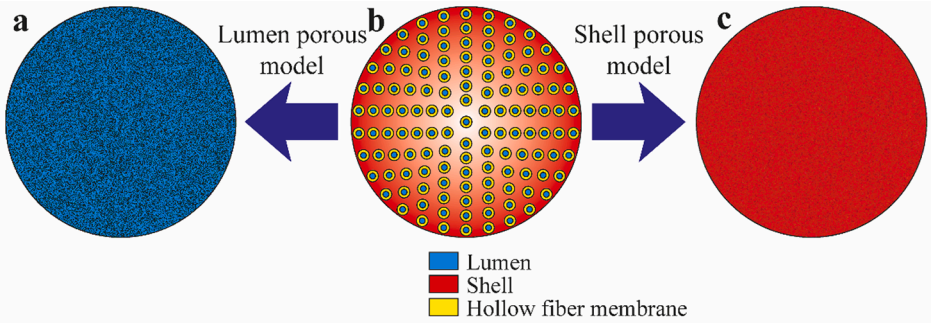

Fig. 1. Illustration of the porous media models. Cross-sections of the module, hollow fiber membranes bundle and of the porous media models for the lumen and shell sides. (a) Porous medium for the lumen side; (b) module and hollow fibers bundle; (c) Porous medium for the shell side.

2.2. Fluid flow model

The Darcy law for anisotropic porous media is considered an appropriate model for the fluid flow inside the vessel containing the membrane bundle [41], in the form:

$$\nabla\cdot\mathbf{u}_\gamma = 0 \tag{3a}$$

$$\mathbf{u}_\gamma = -\frac{\mathbf{K}_\gamma}{\mu_\gamma}\cdot\nabla p_{f,\gamma} \tag{3b}$$

where $\mathbf{u}_\gamma$ is the phase average velocity, $p_{f,\gamma}$ is the intrinsic phase average pressure, μ_γ is the dynamic viscosity of the fluid, and $\mathbf{K}_\gamma$ is the permeability tensor. It is assumed in Eq. (3a) that the mass flow in each side is constant along the module; this hypothesis is common in membrane distillation models [36,37] and quantitative justification for it is given further in the text. The boundary conditions are given by,

$$\mathbf{u}_\gamma = \mathbf{u}_{e,\gamma},\ \text{at the entrance} \tag{4a}$$

$$\mathbf{u}_\gamma\cdot\mathbf{n} = 0,\ \text{at the wall} \tag{4b}$$

where $\mathbf{u}_{e,\gamma}$ is the phase average entrance velocity and $\mathbf{n}$ is an outward drawn unit vector.

Assuming the flow is fully developed and axisymmetric, the axial phase average velocity component is constant (plug flow). Invoking the mass conservation principle, the uniform axial component of the phase average velocity is written as:

$$u_\gamma = (-1)^m\frac{Q_\gamma}{\pi {r_v}^2} \tag{5}$$

where u_γ is the axial component of the phase average velocity, Q_γ is the volume flow rate, r_v is the radius of the vessel.

2.3. Heat transfer model

The proposed model of steady state convective-diffusive heat transfer phenomena in the porous media, valid for the domains depicted in Fig. 2.a,b, is [42]:

$$\rho_\gamma c_{p,\gamma}\mathbf{u}_\gamma\cdot\nabla T_\gamma = \nabla\cdot[k_\gamma\varepsilon_\gamma\nabla T_\gamma] - a_\gamma h_\gamma\left(T_\gamma - T_{m,\gamma}\right) \tag{6}$$

where ρ_γ is the density of water, $c_{p,\gamma}$ is the specific heat at constant pressure of water, k_γ is the thermal conductivity of water, T_γ is the intrinsic average temperature of phase γ, $T_{m,\gamma}$ is the temperature at the interface between the hollow fiber membrane and phase γ, and h_γ is the heat transfer coefficient. Considering the external walls are thermally insulated, the boundary conditions are given by:

$$T_\gamma = T_{e,\gamma},\ \text{at the entrance} \tag{7a}$$

$$\nabla T_\gamma\cdot\mathbf{n} = 0,\ \text{at the wall and outlet} \tag{7b}$$

where $T_{e,\gamma}$ is the temperature profile at the entrance.

Assuming that the porous media are homogeneous, the temperature field is axisymmetric, the Péclet number is sufficiently high to neglect axial conduction [43], and that the thermophysical properties of water are constant, the model of Eq. (6), in cylindrical coordinates, simplifies to:

$$\rho_\gamma c_{p,\gamma}u_\gamma\frac{\partial T_\gamma}{\partial z} = \frac{k_\gamma\varepsilon_\gamma}{r}\frac{\partial}{\partial r}\left(r\frac{\partial T_\gamma}{\partial r}\right) - a_\gamma h_\gamma\left(T_\gamma - T_{m,\gamma}\right) \tag{8}$$

where z is the axial coordinate and r is the radial coordinate. Assuming the temperature at the entrance is uniform, the boundary conditions of Eq. (7a, 7b), in cylindrical coordinates, become:

$$T_\gamma(r, mL) = T_{e,\gamma} \tag{9a}$$

$$\left.\frac{\partial T_\gamma}{\partial r}\right|_{r=0} = 0;\ \left.\frac{\partial T_\gamma}{\partial r}\right|_{r=r_v} = 0 \tag{9b}$$

To further simplify the heat transfer model, note that the boundary conditions in eqs. (9b) impose symmetry and adiabatic conditions at the center and inner surface of the module. In addition, the properties, velocity and entry condition in eqs. (8) and (9a) are independent of the radial direction. The combination of these two facts causes a uniform temperature profile in the radial direction, yielding,

$$\rho_\gamma c_{p,\gamma}u_\gamma\frac{dT_\gamma}{dz} = -a_\gamma h_\gamma\left(T_\gamma - T_{m,\gamma}\right) \tag{10a}$$

with boundary condition given by,

$$T_\gamma(mL) = T_{e,\gamma} \tag{10b}$$

Defining the following dimensionless variables,

$$z^* = \frac{2z}{Per_v};\ u_\gamma^* = \frac{u_\gamma}{u_c};\ T_\gamma^* = \frac{T_\gamma - T_{e,l}}{T_{e,s} - T_{e,l}};\ \rho_\gamma^* c_{p,\gamma}^* = \frac{\rho_\gamma c_{p,\gamma}}{\rho_c c_{p,c}};\ k_\gamma^* = \frac{k_\gamma}{k_c}$$

$$T_{m,\gamma}^* = \frac{T_{m,\gamma} - T_{e,l}}{T_{e,s} - T_{e,l}};\ Pe = \frac{2\rho_c c_{p,c}u_c r_v}{k_c};\ Nu_\gamma = \frac{2h_\gamma r_\gamma}{k_\gamma}$$

where the characteristic phase average velocity, density, specific heat, and thermal conductivity are defined as,

$$u_c = \frac{Q_l + Q_s}{2\pi {r_v}^2};\ \rho_c = \frac{\rho_s + \rho_l}{2};\ c_{p,c} = \frac{c_{p,s} + c_{p,l}}{2};\ k_c = \frac{k_s + k_l}{2}$$

Employing the relations of Eq. (12.a-l), results in the following dimensionless form of Eqs. (10.a,b) (more details on the steps of the derivation can be found in Mendeley Data [44]):

$$\rho_\gamma^* c_{p,\gamma}^* u_\gamma^*\frac{dT_\gamma^*}{dz^*} = -k_\gamma^* N_{fbr} Nu_\gamma\left(T_\gamma^* - T_{m,\gamma}^*\right) \tag{13a}$$

with boundary conditions given by,

$$T_\gamma^*(mL^*) = m \tag{13b}$$

Correlations for the Nusselt number in the lumen and shell sides are taken from the literature [45,46] to close the model of Eqs. (13.a,b) in the form:

$$Nu_\gamma = \begin{cases} \left(4.36 + \dfrac{0.036 Re_\gamma Pr_\gamma\left(d_{h,\gamma}/L\right)}{1 + 0.0011\left[Re_\gamma Pr_\gamma\left(d_{h,\gamma}/L\right)\right]^{2/3}}\right)\left[\dfrac{1 + N_{fbr}(r_s/r_v)}{1 - N_{fbr}(r_s/r_v)^2}\dfrac{r_s}{r_v}\right]^m, & Re_\gamma < 2100 \\ \dfrac{(Re_\gamma - 1000)Pr_\gamma}{1.07 + 12.7\left(Pr_\gamma^{2/3} - 1\right)(f_\gamma/8)^{1/2}}\dfrac{f_\gamma}{8}\left[\dfrac{1 + N_{fbr}(r_s/r_v)}{1 - N_{fbr}(r_s/r_v)^2}\dfrac{r_s}{r_v}\right]^m, & Re_\gamma \geqslant 2100 \end{cases} \tag{14}$$

where Re_γ is the Reynolds number based on the hydraulic diameter $d_{h,\gamma}$,

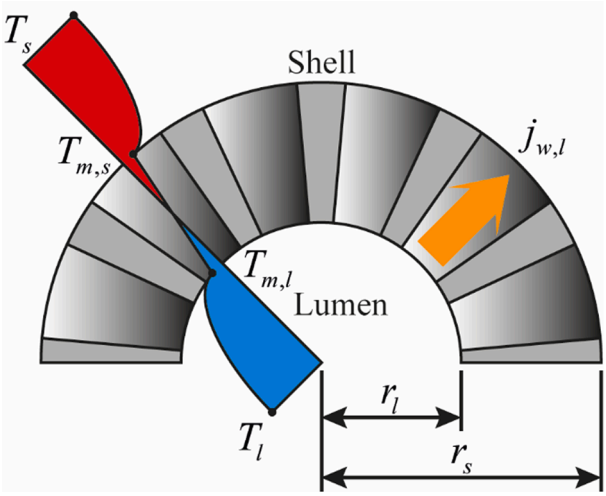

Fig. 3. Illustration of half of the hollow fiber membrane. Out of scale. The temperature profile, the sign convention for the distilled water flux and the dimensions of the membrane cross-section are included.

and Pr_γ is the Prandtl number. The friction factor f_γ and the hydraulic diameters are determined by,

$$f_\gamma = [1.82log(Re_\gamma) - 1.64]^{-2} \tag{15a}$$

$$d_{h,l} = 2r_l;\ d_{h,s} = 2r_v\frac{1 - N_{fbr}(r_s/r_v)^2}{1 + N_{fbr}(r_s/r_v)} \tag{15b,c}$$

Fig. 3 illustrates the heat and mass transport through the membrane. Convection is imposed on both the shell and lumen sides. Within the membrane, heat conduction and water vaporization, transport and condensation are assumed to occur. The water flux $j_{w,l}$ will be assumed positive when occurring from lumen to shell and negative otherwise, in order to comply with the sign convention adopted by the Dusty Gas Model (DGM) to be detailed in section 2.4.

The heat transferred through the membrane is determined in the following way:

$$\dot{q} = \frac{2\pi k_m \Delta z}{ln(r_s/r_l)}\left(T_{m,s} - T_{m,l}\right) - 2\pi r_l \Delta z j_{w,l} h_{fg} \tag{16}$$

where $\dot{q}$ is the local rate of heat transfer, k_m is the thermal conductivity of the membrane, Δz is the length of a portion of the hollow fiber membrane, $j_{w,l}$ is the distilled water flux on the lumen side, $T_{m,s}$ is the temperature at the interface between the membrane and the shell side, $T_{m,l}$ is the temperature at the interface between the membrane and the lumen side, and h_{fg} is the latent heat of vaporization.

For the convection in the lumen and shell sides, the heat transfer coefficients are used to determine the heat transfer rate, as follows:

$$\dot{q} = 2\pi r_s \Delta z h_s\left(T_s - T_{m,s}\right) = 2\pi r_l \Delta z h_l\left(T_{m,l} - T_l\right) \tag{17a,b}$$

where h_s is the heat transfer coefficient on the shell side and h_l is the heat transfer coefficient on the lumen side.

After algebraic manipulation of Eqs. (16) and (17.a,b), the following equations can be used to find the temperatures at each border of the membrane:

$$T_{m,s} = T_s - \left\{1 + \frac{r_s h_s\left(T_{m,s} - T_{m,l}\right)ln(r_s/r_l)}{k_m\left(T_{m,s} - T_{m,l}\right) - j_{w,l}h_{fg}r_l ln(r_s/r_l)} + \frac{r_s h_s}{r_l h_l}\right\}^{-1}(T_s - T_l) \tag{18a}$$

$$T_{m,l} = T_l + \left\{1 + \frac{r_l h_l\left(T_{m,s} - T_{m,l}\right)ln(r_s/r_l)}{k_m\left(T_{m,s} - T_{m,l}\right) - j_{w,l}h_{fg}r_l ln(r_s/r_l)} + \frac{r_l h_l}{r_s h_s}\right\}^{-1}(T_s - T_l) \tag{18b}$$

The isostrain model [30,33], which is expected to work well for membranes with solid and gaseous phases approximately parallel to each other, shall be adopted for the thermal conductivity of the membrane, yielding:

$$k_m = k_v\varepsilon_m + (1 - \varepsilon_m)k_p \tag{19}$$

where k_v is the thermal conductivity of the air-vapor mixture, k_p is the thermal conductivity of the polymer, and ε_m is the porosity of the membrane.In order to obtain a dimensionless form of Eq. (18.a,b), the following dimensionless groups are defined:

$$j^*_{w,l} = \frac{c_{p,c}r_v j_{w,l}}{k_c};\ h^*_{fg} = \frac{h_{fg}}{c_{p,c}\left(T_{e,s} - T_{e,l}\right)};\ k^*_m = \frac{k_m}{k_c} \tag{20a–c}$$

Substituting Eqs. (20a) and (12.a-l) into Eqs. (18.a,b), we then have,

$$T^*_{m,s} = T^*_s - \left\{1 + \frac{Nu_s k^*_s\left(T^*_{m,s} - T^*_{m,l}\right)ln\left(r^*_s/r^*_l\right)}{2k^*_m\left(T^*_{m,s} - T^*_{m,l}\right) - 2j^*_{w,l}h^*_{fg}r^*_l ln\left(r^*_s/r^*_l\right)} + \frac{Nu_s k^*_s}{Nu_l k^*_l}\right\}^{-1}\left(T^*_s - T^*_l\right) \tag{21a}$$

$$T^*_{m,l} = T^*_l + \left\{1 + \frac{Nu_l k^*_l\left(T^*_{m,s} - T^*_{m,l}\right)ln\left(r^*_s/r^*_l\right)}{2k^*_m\left(T^*_{m,s} - T^*_{m,l}\right) - 2j^*_{w,l}h^*_{fg}r^*_l ln\left(r^*_s/r^*_l\right)} + \frac{Nu_l k^*_l}{Nu_s k^*_s}\right\}^{-1}\left(T^*_s - T^*_l\right) \tag{21b}$$

2.4. Mass transfer model

For DCMD, the influence of the concentration polarization is usually small for salinities below 5 wt% [11], thus the salt concentration is regarded as uniform in the feed-side flow. The Dusty Gas Model (DGM) shall be employed to model the mass transport, since it has been shown to correctly predict distilled water fluxes for DCMD applications [29]. Assuming the surface diffusion is small [47] and the viscous transport mechanism is negligible for DCMD [29], the DGM becomes:

$$\frac{N_w}{D^k_w} + \frac{p_a N_w - p_w N_a}{D^0_{wa}} = -\frac{1}{RT_m}\nabla p_w \tag{22}$$

where N_w is the molar flux of water vapor, N_a is the molar flux of air, p_a is the partial pressure of air within the pore, p_w is the partial pressure of water vapor within the pore, D^k_w is the Knudsen diffusivity of water vapor, D^k_a is the Knudsen diffusivity of air, D^0_{wa} is the molecular diffusivity of water vapor in air, D^0_{aw} is the molecular diffusivity of air in water vapor, R is the universal gas constant, and T_m is the average temperature along the membrane.

The air can then be considered to be approximately quiescent within the membrane pores, i.e., $N_a \cong 0$ [30]. We then have,

$$\frac{N_w}{D^k_w} + \frac{p_a N_w}{D^0_{wa}} = -\frac{1}{RT_m}\nabla p_w \tag{23}$$

Employing Dalton's law in Eq. (23) and integrating, yields,

$$N_{w,l} = \frac{D^0_{wa}}{RT_m r_l ln(r_s/r_l)}ln\left(\frac{D^0_{wa} - D_{eff}p_s}{D^0_{wa} - D_{eff}p_l}\right) \tag{24}$$

where $N_{w,l}$ is the molar flux of distilled water based on the inner area of the hollow fiber membrane, D_{eff} is the effective diffusivity, p_s is the partial pressure of water vapor at the interface between the membrane

and the shell side, and p_l is the partial pressure of water vapor at the interface between the membrane and the lumen side.

The diffusivities can be obtained from the relations below [33]:

$$D_{wa}^{0} = 4.46 \times 10^{-6} \frac{\varepsilon_m}{\tau_m} T_m^{2.334} \tag{25a}$$

$$D_{w}^{k} = \frac{\varepsilon_m}{\tau_m} \frac{d_p}{3} \sqrt{\frac{8RT_m}{\pi M_w}} \tag{25b}$$

$$D_{eff} = \frac{D_w^k D_{wa}^0}{D_{wa}^0 + PD_w^k} \tag{25c}$$

where τ_m is the membrane tortuosity, d_p is the mean membrane pore diameter, M_w is the molecular weight of water, and where P is the total pressure within the membrane pores. The tortuosity is given by [33],

$$\tau_m = \frac{1}{\varepsilon_m} \tag{26}$$

The partial pressures of water vapor at the interfaces can be determined from the vapor pressure at the particular interface temperature and an activity coefficient in the following way [33]:

$$p_\gamma = \left(1 - x_{salt,\gamma}\right) \alpha_\gamma p_{v,\gamma} \tag{27a}$$

with activity coefficients given by,

$$\alpha_\gamma = 1 - 0.5 x_{salt,\gamma} - 10 x_{salt,\gamma}^2 \tag{27b}$$

where $x_{salt,\gamma}$ is the molar fraction of salt at the stream γ, α_γ is the activity coefficient, and $p_{v,\gamma}$ is the vapor pressure at the interface between the membrane and the stream γ. The expression for the activity coefficient was fitted to experimental data for salinities up to 29 wt% [48,49]. The vapor pressures are read and interpolated from tables available in the literature [49].

Finally, the distilled water mass flux can be determined from its molar counterpart as follows:

$$j_{w,l} = M_w N_{w,l} \tag{28}$$

2.5. Computational procedure

A computational code was developed using Wolfram Mathematica v.11 [50]. More details on the computational procedure are available as supplementary information in Mendeley Data [44]. All thermophysical properties for salt water that are used in the results presented further in the text are taken from correlations and tables available in the literature [49,51]. The developed code takes at most 6 min to run in an Intel Core i7-4510U, 8 GB RAM notebook.

2.6. Post-processing

The average distilled water flux is determined in the following way:

$$\bar{j}_{w,l} = \left| \frac{1}{L} \int_0^L j_{w,l} dx \right| \tag{29}$$

where $\bar{j}_{w,l}$ is the average distilled water flux.

The gain-output ratio for membrane distillation systems is defined as the quotient between the latent heat carried by the vapor as it is transported through the membrane and the total heat added to the system [12,52]. Mathematically,

$$GOR = \frac{\dot{q}_v}{\dot{q}_h} \tag{30a}$$

with,

$$\dot{q}_v = \left| \int_0^L 2\pi N_{fbr} r_l j_{w,l} h_{fg} dz \right| \tag{30b}$$

where GOR is the gain-output ratio, $\dot{q}_v$ is the total heat carried through the membrane by the vapor, and $\dot{q}_h$ is the heat added.

For a system without heat recovery, the energy conservation principle demands that the gain-output ratio be always less than unity, which renders a high energy consumption of the MD process [12]. To partially offset this energy expenditure, a heat recovery system can be integrated with the desalination module such as the one shown in Fig. 4. The presence of the heat recovery system helps to justify the choice of GOR as a figure-of-merit over thermal efficiency which is the ratio between heat carried by the vapor and the total heat transferred through the membrane; the latter figure is independent of the external heat

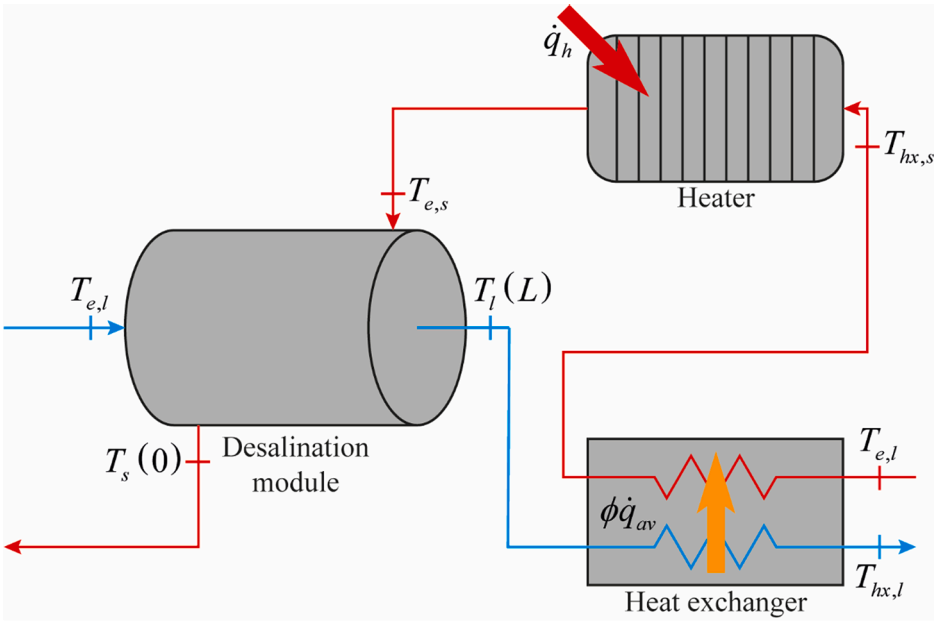

Fig. 4. Desalination system with external heat exchanger for heat recovery.

recovery. Nevertheless, thermal efficiencies are calculated for the sake of completeness (see spreadsheet in Mendeley Data [44])

The system shown in Fig. 4 assumes the hot feed flows in the shell and this configuration shall be adopted in this work. Heat recovery is achieved through an external heat exchanger responsible for pre-heating the feed stream with available heat from the outlet of the permeate stream. For this particular case, the gain-output ratio is expressed as follows [53]:

$$GOR = \frac{\dot{q}_v}{\dot{q}_t - \phi \dot{q}_{av}} \tag{31a}$$

with,

$$\dot{q}_t = \rho_s Q_s c_{p,s} \left(T_{e,s} - T_{e,l}\right) \tag{31b}$$

$$\dot{q}_{av} = min\left(\rho_s Q_s c_{p,s}, \rho_l Q_l c_{p,l} + 2\pi N_{fbr} r_l L \bar{j}_{w,l} c_{p,l}\right)\left[T_l(L) - T_{e,l}\right] \tag{31c}$$

where $\dot{q}_t$ is the heat transfer necessary to elevate the feed from the ambient temperature (assumed to be equal to the lumen inlet temperature) to the shell inlet temperature, $\dot{q}_{av}$ is the maximum possible heat transfer in the heat exchanger, and ϕ is the effectiveness of the heat exchanger. The specific energy consumption (SEC), which is directly proportional to the latent heat of vaporization and inversely proportional to the GOR is also provided as supplementary data for all simulation runs (see spreadsheet in Mendeley Data [44]).

For plug flow, Eq. (3.b) gives the pressure loss, which can be written as,

$$\Delta p_{f,\gamma} = \frac{\mu_\gamma}{K_{x,\gamma}} |u_\gamma| = \frac{\mu_\gamma}{K_{x,\gamma}} \frac{Q_\gamma}{\pi {r_v}^2} \tag{32}$$

where $K_{x,\gamma}$ is the permeability in the longitudinal direction. The permeabilities are obtained through a correlation for the shell side [54] and using Poiseuille flow for the lumen side, as follows:

$$K_{x,s} = -\frac{{r_s}^2}{8(1-\varepsilon_s)}\left[2ln(1-\varepsilon_s) + 2\varepsilon_s + {\varepsilon_s}^2\right] \tag{33a}$$

$$K_{x,l} = \frac{\varepsilon_l {r_l}^2}{8} \tag{33b}$$

Laminar flow is assumed in Eqs. (33.a,b), which is justified by the Reynolds numbers of the cases analyzed (see Mendeley Data [44]). The product of the pressure drop by the associated flow rate yields the pumping power.

A figure-of-merit, analogous to the GOR, will be used to evaluate the relative importance of the pumping power. This figure-of-merit is named mechanical gain-output ratio (MGOR), emphasizing its relation to the mechanical energy expenditure to overcome the pressure losses along the module. MGOR is defined as the quotient between the latent heat carried by the water vapor through the membrane and the total pumping power, i.e., the sum of the pumping power through both the lumen and shell sides. Thus,

$$MGOR = \frac{\dot{q}_v}{\dot{W}_p} = \frac{\dot{q}_v}{Q_l \Delta p_{f,l} + Q_s \Delta p_{f,s}} \tag{34}$$

where $\dot{W}_p$ is the total pumping power.

3. Results and discussion

3.1. Validation of the code and assessment of the model

Before proceeding with the analysis of the MD modules, validation of the model and code developed is carried out. Two sets of results are used for this purpose, both stemming from experimental works published in the literature [25,55]. Two independent results were used to eliminate the possibility of the agreement between the numerical and experimental results being restricted to a particular membrane or module. Fig. 5.a,b present the water flux as a function of the feed temperature for these experimental results, compared with numerical results from this work and others from the literature [34,36,37]. In both cases, the results from this work are closer to the experimental ones. A more significant deviation from the experimental results is observed for higher feed temperatures, which can be attributed to the hypothesis of isothermal transport used in the DGM. In addition, Fig. 5.a shows an abrupt increase in the water flux predicted with the model and methodology here developed for a temperature close to 50 °C; this fact is due to the transition to turbulence associated with the lower fluid viscosity for higher temperatures. Previous efforts limit their analyses to laminar flows [36,37], which is a likely explanation for the larger gap between these results and the experimental ones in the range from 50 °C to 70 °C.

To further demonstrate the adequacy of the proposed model, Table 1 presents a comparison between the results of the porous media model and experimental results from the literature [55] for the feed and permeate temperatures at the outlet. The relative difference between the numerical and experimental values is within 5% for all cases, except for the permeate outlet temperature when the feed temperature is 79.3 °C. This inaccuracy for high feed temperatures was already discussed in the context of Fig. 5.a.

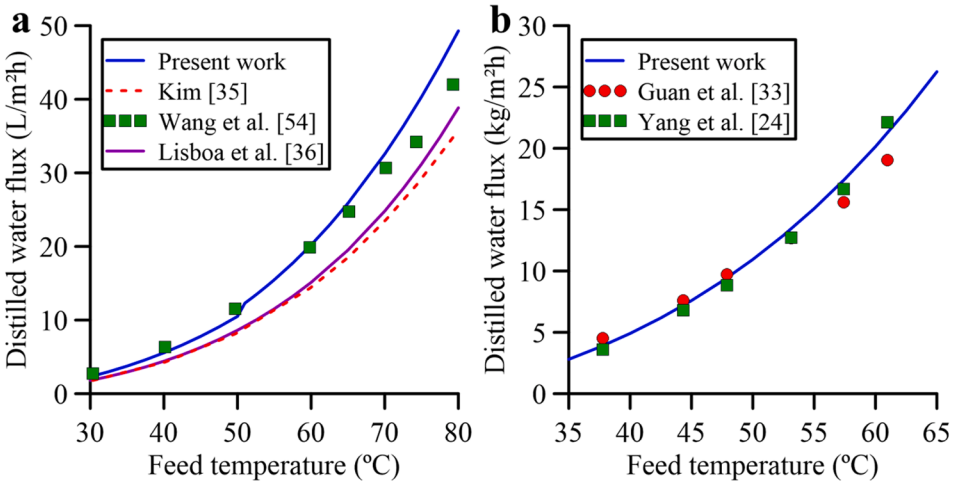

Fig. 5. Comparison of the distilled water flux as a function of the feed temperature with experimental and numerical results from the literature. Comparison with: (a) Kim [36] (numerical), Wang et al. [55] (experimental), and Lisboa et al. [37] (numerical); (b) Guan et al. [34] (numerical), Yang et al. [25] (experimental).

Table 1
Comparison of the feed and permeate outlet temperatures of the porous media model with experimental results from the literature [55]. The permeate inlet temperature is 17.5 °C for all cases.

Feed inlet temperature (°C)	Feed outlet temperature (°C)			Permeate outlet temperature (°C)		
	Present work	Experimental [55]	Relative difference	Present work	Experimental [55]	Relative difference
40.0	38.5	39.0	1.28%	23.4	24.5	4.49%
49.5	47.2	48.0	1.67%	26.5	27.8	4.68%
59.8	56.2	57.4	2.09%	31.7	31.3	1.28%
70.2	65.1	67.2	3.13%	37.5	36.2	3.59%
79.3	72.6	76.0	4.47%	43.8	39	12.3%

Table 2
Parameters for the base case of the model for DCMD with heat recovery.

Parameter	Symbol	Value	Unit	Label
Internal radius of the membrane	r_l	0.3	mm	A
Thickness of the membrane	t	0.1	mm	B
Conductivity of the polymer	k_p	0.2	W/mK	C
Pore diameter	d_p	0.2	μm	D
Membrane porosity	ε_m	0.8	–	E
Inlet temperature in the shell side	$T_{e,s}$	60	°C	–
Inlet temperature in the lumen side	$T_{e,l}$	25	°C	–
Total pressure in the membrane pores	P	101.325	kPa	
Flow rate in the shell side	Q_s	50	L/min	–
Flow rate in the lumen side	Q_l	50	L/min	–
Number of hollow fibers	N_{fbr}	10,000	–	–
Radius of the vessel	r_v	50	mm	–
Effective length of the vessel	L	1	m	–
Molar fraction of salt in the shell side	$x_{salt,s}$	0.011	–	–
Molar fraction of salt in the lumen side	$x_{salt,l}$	0	–	–

Besides the improved agreement with experiments, the use of the porous media approach offers the possibility of relaxing some of the simplifying assumptions made. For instance, heat losses to the environment are easy to be included in eq. (7.b); this effect is necessarily absent when the single representative fiber model is considered [36,37]. Furthermore, the model can be extended to account for heterogeneities within the porous media through variable properties [41,42], allowing for non-uniform distribution of fibers along the cross-section to be modeled.

3.2. Assessment of the membrane influence on the energy efficiency

Table 2 presents the base values for all membrane parameters, which are typical of DCMD applications [25,55]. Letters from A to E are associated with each membrane parameter for labeling purposes. In addition, values for the operational parameters used in the remainder of the work are also presented. For the design matrix of the 2^n experiment planning scheme [56], values for the membrane parameters corresponding to 90% and 110% of the base value act as lower and higher levels, respectively. For the five membrane factors analyzed, 32 simulation runs are performed in accordance with the design matrix (see Mendeley Data [44]).

The effects of each parameter and their interactions on the gain-output ratio are calculated [56] and organized in Pareto charts for different values of the effectiveness of the heat exchanger in Fig. 6, including the ideal case of an infinitely large heat exchanger operating in countercurrent configuration ($\phi = 1$). More details on how the effects of each parameter or interaction of parameters are calculated are supplied as Supplementary Information (see Mendeley Data [44]). Only eight parameters or combination of parameters are contemplated in the charts for the sake of conciseness.

According to Fig. 6, the membrane porosity is the most important parameter for all values of the heat exchanger effectiveness, which can be attributed to the influence of the porosity on both minimizing parasitic conductive losses and improving membrane permeability. The great sensitivity of the energy efficiency of membrane distillation modules to the porosity was already reported in the literature [30], which corroborates the findings presented in Fig. 6.

The thermal conductivity of the polymer used in the membrane manufacturing is very important for applications with no heat recovery or using small heat exchangers. However, the conductivity loses importance for effectiveness closer to 1. A possible explanation is that a significant part of the conductive heat loss is recovered with a highly effective heat exchanger. A question might arise as to whether the water productivity is compromised by employing higher thermal conductivities. When one compares the water flux for the lower level of thermal conductivity with the water flux for the higher level (cases 28 and 32 of the design matrix; see Mendeley Data [44]), the latter still amounts to 97% of the former, despite the 22% increase in thermal conductivity. Therefore, the possible negative effects on productivity are considered to be negligible for the range here analyzed.

The internal radius of the membrane becomes increasingly important with higher heat exchanger effectiveness, coming relatively close to the membrane porosity in terms of effect over the gain-output ratio. The gains in GOR with higher internal radius of the fibers can be explained by the increase in area available for heat and mass transfer. The irreversibilities along the membranes are reduced with smaller temperature differences, thereby increasing the usefulness of the effluent from the lumen side possibly turning the internal radius into a major factor for ϕ closer to unity.

The thickness is recognized to have a neutral effect on the energy efficiency of the membrane [11,30]. In this case, the negative effect of having more conductive losses with thinner membranes is offset by the associated increase in permeability. This trend is expected for a stand-alone module with no heat recovery, and Fig. 6.a shows that the effect of the membrane thickness in this situation is negligible. The importance of the thickness for the gain-output ratio increases for more effective heat exchangers. However, the effect of thicker membranes is the reduction of the energy efficiency, indicating that the negative effect on the membrane permeability prevails over the increase in surface area and the decrease in heat conduction losses.

The mean pore diameter maintains roughly the same importance as far as the gain-output ratio is concerned, regardless of the effectiveness of the heat exchanger. The improvement in permeability it offers is always beneficial.

The interactions between membrane parameters are mostly secondary for every value of heat exchanger effectiveness tested. Given the limitations of the various manufacturing techniques available, often being unable to control a certain parameter and/or demanding trade-offs between these variables [26], the fact that the interactions of two or more membrane parameters have a weak effect on the gain-output ratio is an advantage. From the results of Fig. 6, the emphasis should be on maximizing porosity, favoring techniques such as electrospinning of nanofibers [26]. Furthermore, for very efficient heat recovery systems, the importance of employing a low thermal conductivity material to manufacture the membrane diminishes, which might convert immobilized carbon nanotubes membranes into a viable option [26].

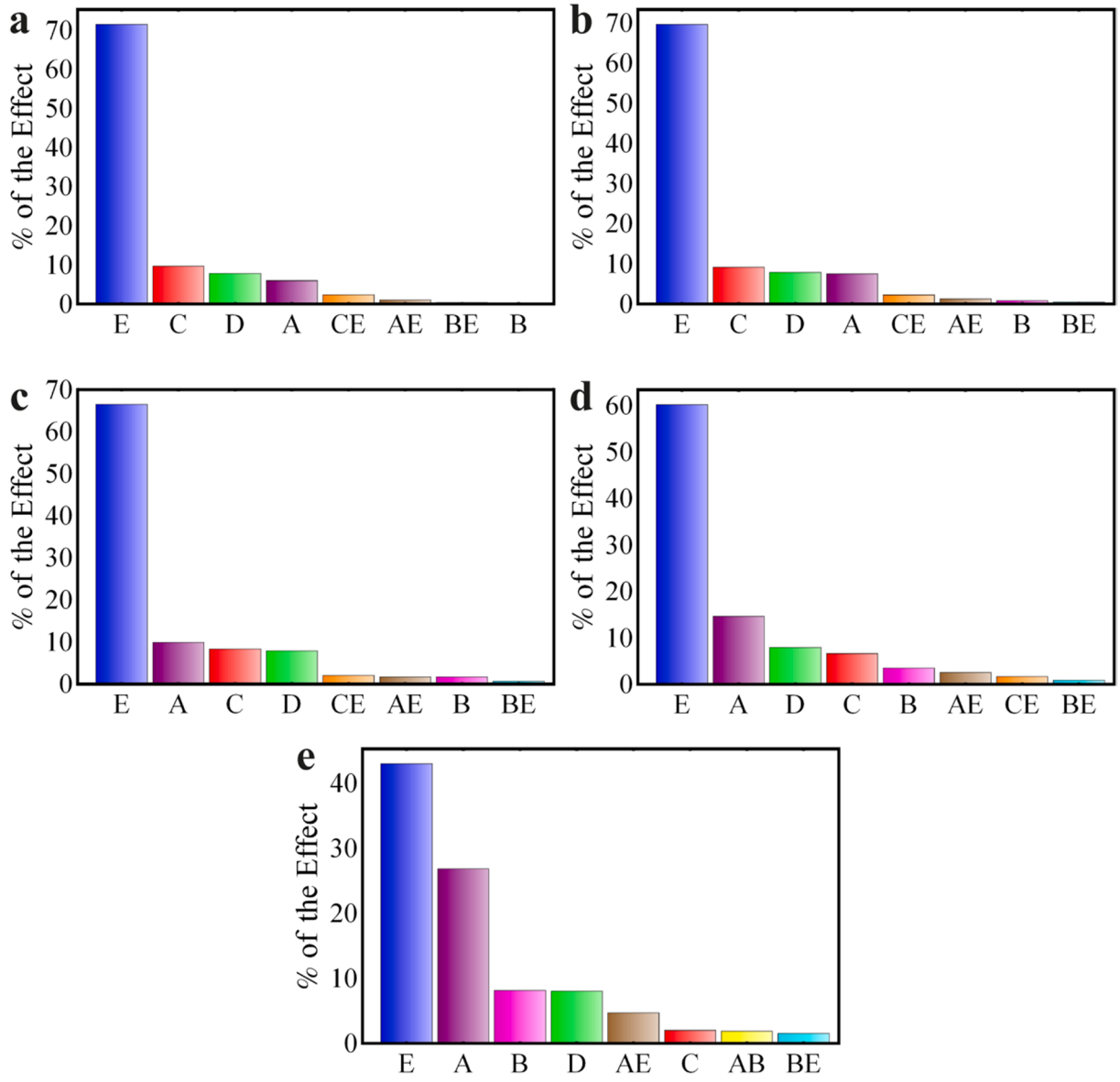

Fig. 6. Pareto charts of the effects of the membrane parameters on the gain-output ratio. Heat exchanger effectiveness: (a) $\phi = 0$ (no heat recovery); (b) $\phi = 0.25$; (c) $\phi = 0.5$; (d) $\phi = 0.75$; (e) $\phi = 1$. Labels: A – internal radius of the membrane; B – thickness of the membrane; C – conductivity of the polymer; D – pore diameter; E – membrane porosity. Combination of two letters stands for the interaction between two parameters (e.g., AE refers to the effect of the interaction between the internal radius and the porosity). For the calculation procedure used and the specific values of the effects consult the supplementary information file and the design matrix spreadsheet in Mendeley Data [44].

Amongst the cases simulated, the maximum energy efficiency, measured by the gain-output ratio, was achieved for internal radius, pore diameter and porosity at the upper levels (110% of the base value of Table 2), while the thickness and the thermal conductivity were at their lower levels (90% of the base value of Table 2). For the ideal case of $\phi = 1$, the GOR is equal to 4.85, which is equivalent to specific energy consumption (SEC) of 495 kJ/kg (or 137 kWh/m^3). This figure is similar to previously reported SECs for small scale systems [12].

Given the focus of the factorial analysis on the membrane characteristics, no correlation of the GOR with membrane-related parameters is offered, for it would be overly specific to the operational parameters and size of the system under analysis, thereby limiting its usefulness.

The effects of the three most important membrane parameters for the ideal case of an infinitely large heat exchanger, namely membrane porosity, internal radius and thickness, shall be investigated further in the upcoming sections.

3.3. Influence of the membrane porosity

Fig. 7.a shows the influence of the membrane porosity on the gain-output ratio for four different values of the effectiveness of the heat exchanger. In the range studied, the four graphs present only a slight curvature, closely resembling linear curves. For all cases, porosities as close as possible to 1 are desirable, limited by the capabilities of the manufacturing process and the structural integrity of the membrane [26]. Comparing the curve for the ideal case of $\phi = 1$ with the others, the high sensitivity of the GOR to the effectiveness of the heat exchanger for $\phi > 0.75$ is evident, allowing for the conclusion that efficient heat recovery is crucial for a successful DCMD system.

Fig. 7.b depicts the water flux and system capacity through the membranes as a function of membrane porosity. The system capacity consists of the total amount of water carried through the membranes per unit of time. The inlet feed temperature is fixed at 60 °C, thus the curves of Fig. 7.b are independent of the heat recovery system. For the case of

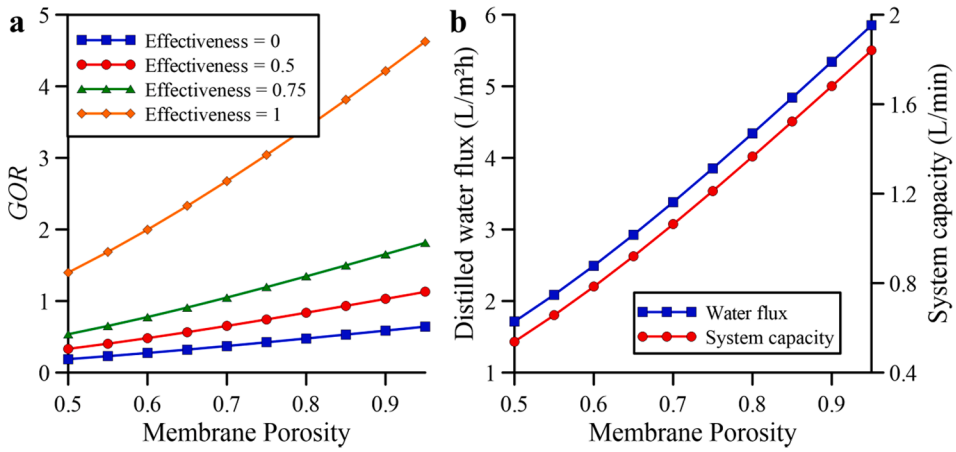

Fig. 7. Variation of the gain-output ratio and water productivity with the membrane porosity. (a) *GOR* as a function of membrane porosity; (b) Distilled water flux and system capacity as a function of membrane porosity.

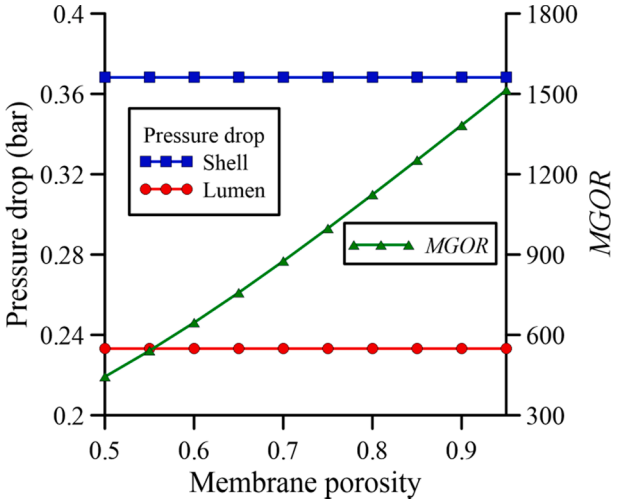

Fig. 8. Pressure drop and MGOR as functions of the membrane porosity.

varying membrane porosity with everything else fixed, the two curves differ only by a constant scale factor. It is clear that higher membrane porosity is advantageous both for energy efficiency and water productivity. In order to evaluate the validity of the assumption of negligible contribution of the flow rate variation along the module, a comparison of the maximum system capacity of Fig. 7.b (~1.8 L/min) is done with the flow rate in both the shell and lumen sides, as given by Table 2. The flow rate variation accounts for at most 3.6% of the inlet flow rate in both the shell and lumen sides, substantiating the modeling choice.

Fig. 8 presents the pressure drop and the MGOR for varying membrane porosity. The pressure drops in both the lumen and shell sides are constant and well below the typical liquid entry pressures (LEP) of polymer membranes for MD applications [26], indicating that pore wetting is unlikely to occur under these conditions. The MGOR increases monotonically with the membrane porosity, indicating a decreasing power cost to produce a given amount of water (see Mendeley Data for values of the pumping power [44]). In particular, for the base case of Table 2, the MGOR is 1124, which is equivalent to a specific mechanical energy consumption of ~ 0.6 kWh/m^3; such value is in the same order of magnitude as previously reported results [35]. A comparison of the MGOR values of Fig. 8 with the GOR values of Fig. 7.a, shows that the thermal energy input far exceeds its mechanical counterpart, corroborating the focus on the GOR in the analysis of section 3.2.

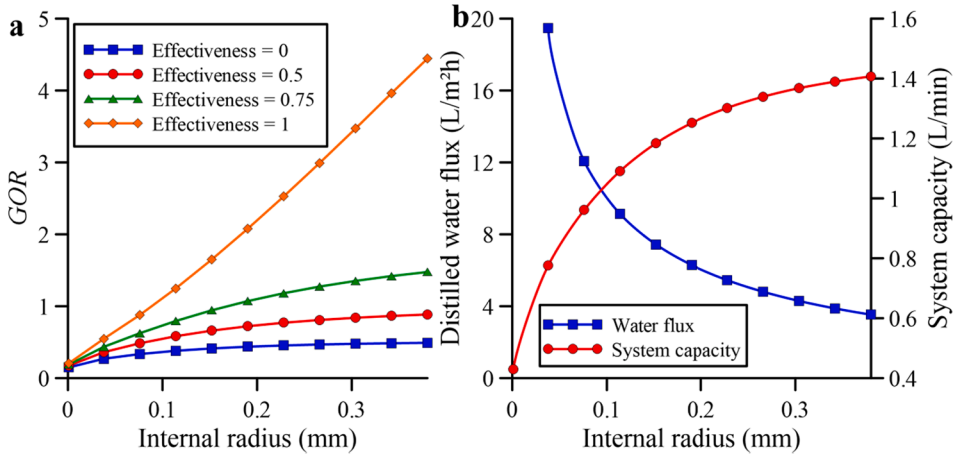

Fig. 9. Variation of the gain-output ratio and water productivity with the internal radius of the membrane. (a) *GOR* as a function of internal radius; (b) Distilled water flux and system capacity as a function of internal radius.

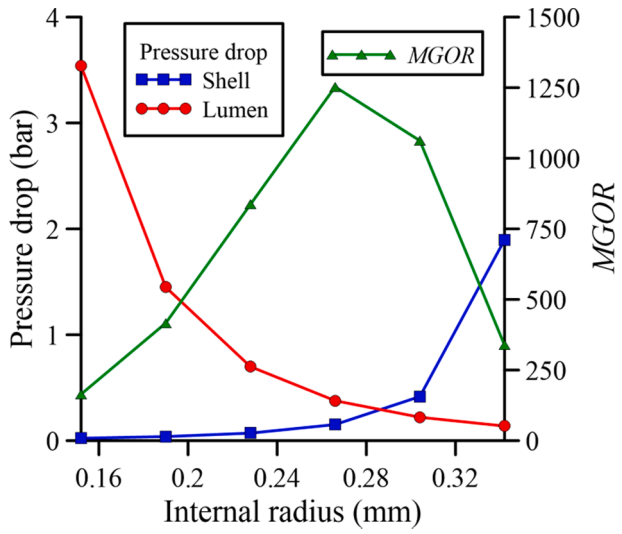

Fig. 10. Pressure drop and MGOR as functions of the internal radius of the membrane.

3.4. Influence of the internal radius of the hollow fiber

Fig. 9.a presents the influence of the internal radius of the membrane on the gain-output ratio. Once more, four values for the heat exchanger effectiveness are considered. The same behavior for $\phi > 0.75$ observed in Fig. 7.a is present, with a great improvement of the sensitivity of the GOR with respect to the internal radius. This behavior reinforces that the most effective way to optimize DCMD systems involves not only the careful design of the membrane and the module, but also the design of the heat recovery. Overall, the internal radius of the hollow fiber improves the energy efficiency of the desalination system, which is attributed to the increase in area available for heat and mass transfer and, consequently, the reduction of the irreversibility in these processes.

Fig. 9.b shows the water flux and system capacity as a function of the internal radius of the membrane. The water flux decreases with increasing internal radius. Analyzing Eqs. (24) and (28), the water flux is expected to decrease with the internal radius due to increasing membrane area. On the other hand, the system capacity, also contemplated in Fig. 9.b, increases with the internal radius. This result shows that the increase in membrane area available is able to compensate the aforementioned negative effects the internal radius has on water flux.

Fig. 10 depicts the pressure drop for the lumen and shell sides and the MGOR for certain values of the internal radius of the membrane. Note that, because the pressure drop of one of the sides of the module soars with either smaller or larger values of the internal radius, the range of internal radius considered in Fig. 10 is reduced in comparison with Fig. 9, for visualization purposes. Furthermore, typical liquid entry pressures of polymeric membranes are 1–4 bar [26]; thus the limits imposed to the range of internal radius are also necessary to avoid pore wetting. Nevertheless, in the range shown, the MGOR exceeds the related GOR by at least two orders of magnitude, indicating that the need for mechanical input is much smaller than the thermal input.

3.5. Influence of the membrane thickness

The membrane thickness effect on the gain-output ratio is shown in Fig. 11.a. Once more, Fig. 11.a shows an abrupt increase of energy efficiency for $\phi > 0.75$. For the case with no heat recovery, the curve is mostly flat, with the exception of the bottom of the range of values for the membrane thickness. Furthermore, an optimum value for the membrane thickness is present for all four heat exchanger effectiveness in Fig. 11.a, in agreement with previously published results [11,12,39,40]. This optimum thickness shifts to lower values with rising heat exchanger effectiveness, possibly due to the partial recovery of the heat conduction losses, allowing for the use of thinner, more permeable membranes. For membranes thinner than ~ 10 μm, a reverse flux, from permeate to feed, was observed as an effect of the small temperature

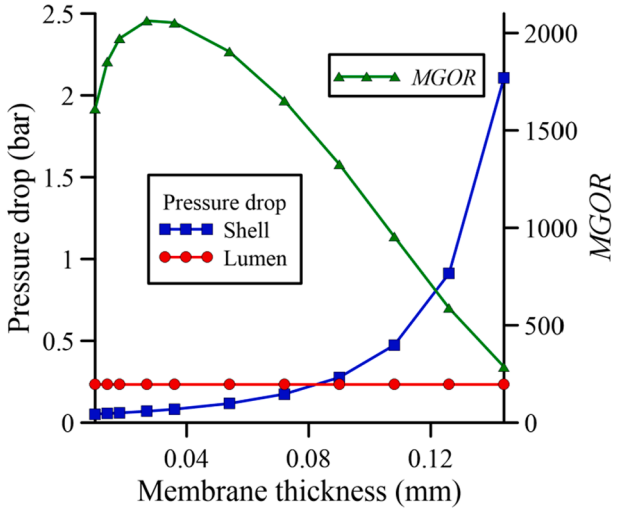

Fig. 12. Pressure drop and MGOR as functions of the membrane thickness.

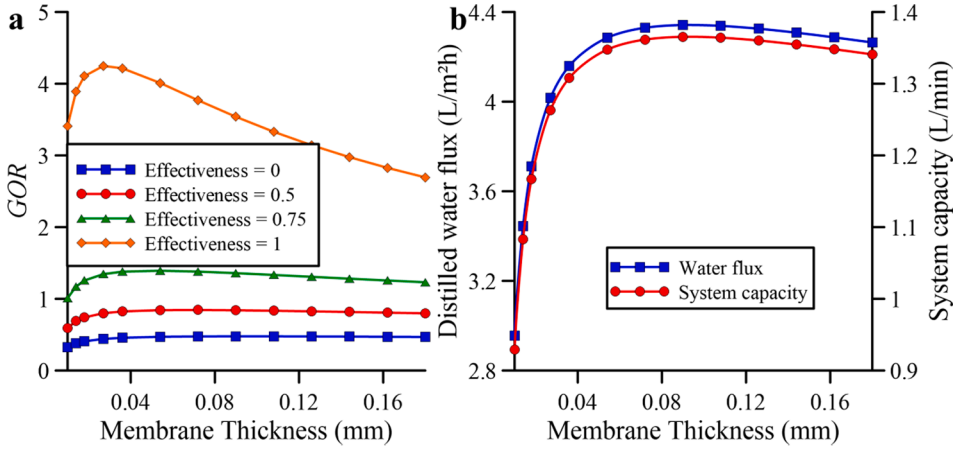

Fig. 11. Variation of the gain-output ratio and water productivity with the thickness of the membrane. (a) *GOR* as a function of membrane thickness; (b) Distilled water flux and system capacity as a function of membrane thickness.

difference not being able to offset the lower activity coefficient of the feed side. Similar observations can be found in the literature [11].

Fig. 11.b show the variation of the water flux and the system capacity with the membrane thickness. Given the independence of the internal membrane area on its thickness, both curves are qualitatively similar and differ only by a constant scale factor. The water productivity curves also present an optimum thickness. Since the inlet temperature at the feed side is fixed, the curves are invariant with the effectiveness of the heat recovery system and, consequently, a single optimum thickness of ~ 90 μm is identified. For membrane thicknesses below 30 μm, the water productivity sharply decreases, as the heat conduction losses compromise the driving force. The decrease in water productivity might increase the need for pumping power input as larger modules would be needed for a given demand for water. To evaluate this possibility, the water flux at optimum thickness for maximum GOR when the heat recovery system effectiveness is 1 is compared with the peak water flux taken from Fig. 11.b, showing that the former is still around 92% of the latter. Therefore, the penalty of seeking maximum GOR in terms of pumping power is expected to be small.

The pressure drop for the shell and lumen side and the MGOR are plotted in Fig. 12 for different values of the membrane thickness. The pressure drop in the lumen is constant, since the internal radius is fixed. On the other hand, the pressure drop in the shell side soars for membrane thicknesses above 100 μm due to the reduced cross-section area available for the feed stream to flow; hence the range of membrane thicknesses in Fig. 12 is smaller than the one presented in Fig. 11. Furthermore, this reduced range is enforced by the LEP, leading to a maximum allowable membrane thickness. At least for the case under analysis, the optimum membrane thicknesses either for maximum GOR or water productivity are smaller than the value of the maximum allowable thickness.

4. Conclusions

A porous media approach to the modeling and simulation of membrane distillation in hollow fiber membranes modules was proposed and validated against both numerical and experimental results from the literature, with satisfactory results. The employment of the porous media model eases the inclusion of turbulence effects, shown to be an important factor depending on the operational parameters, and offers the possibility of analyzing non-uniform distribution of hollow fibers with rather simple additions. Heat losses to the environment, which have recently been shown to have a significant effect on the performance of membrane distillation modules [57], can also be added. Moreover, the mild computational cost of the code developed can be useful for design and optimization of desalination systems.

The model and computational code developed were used to investigate the relative importance of five different membrane parameters and their combinations on the energy efficiency of a desalination system employing a direct contact membrane distillation module and a heat recovery system. The interactions between the parameters were shown to have a weak effect on the gain-output ratio, allowing for emphasis on individual parameters in future membrane development efforts. The membrane porosity was identified as the most important parameter for different effectiveness of the heat recovery system, favoring manufacturing techniques capable of delivering highly porous membranes, such as electrospinning [26].

A sharp rise of the energy efficiency of the desalination system occurs for highly effective external heat recovery systems, leveraging the impact of each parameter studied. In particular, the membrane thickness was shown to have an optimum value dependent on the heat exchanger effectiveness, offering the possibility of applying thinner, more permeable membranes when combined with well-designed heat recovery systems, provided the water productivity is not compromised and pore wetting is avoided.

The results show that joint development of membranes and heat recovery systems are the most effective way to improve the competitiveness of membrane distillation against other thermal-based desalination techniques and to render membrane distillation a commercially viable option for brackish and seawater desalination. Therefore, in addition to membrane development, detailed design and new constructive ideas for the heat recovery system is a line of research worth pursuing.

Declaration of Competing Interest

The authors declare that they have no known competing financial interests or personal relationships that could have appeared to influence the work reported in this paper.

Acknowledgements

The authors are grateful for the financial support offered by the Brazilian Government agencies CNPq, CAPES (PROCAD-Defesa), and FAPERJ (Grant no. E-26/010.002590/2019).

Supplementary data

The supplementary data is available in Mendeley Data (ref. 44) and can be found through the URL: https://doi.org/10.17632/z7y3dt35rc.2.

References

[1] N. Voutchkov, Energy use for membrane seawater desalination – current status and trends, Desalination 431 (2018) 2–14, https://doi.org/10.1016/j.desal.2017.10.033.
[2] S.M. Shalaby, Reverse osmosis desalination powered by photovoltaic and solar Rankine cycle power systems: A review, Renew. Sust. Energ. Rev. 73 (2017) 789–797, https://doi.org/10.1016/j.rser.2017.01.170.
[3] T.-S. Chung, L. Luo, C.F. Wan, Y. Cui, G. Amy, What is next for forward osmosis (FO) and pressure retarded osmosis, Sep. Purif. Technol. 156 (2015) 856–860, https://doi.org/10.1016/j.seppur.2015.10.063.
[4] S. Porada, W.J. van Egmond, J.W. Post, M. Saakes, H.V.M. Hamelers, Tailoring ion exchange membranes to enable low osmotic water transport and energy efficient electrodialysis, J. Membr. Sci. 552 (2018) 22–30, https://doi.org/10.1016/j.memsci.2018.01.050.
[5] G. Mantero, G. Lomonaco, R. Marotta, Nuclear desalination: An alternative solution to the water shortage, Glob. J. Energy Technol. Res. Updates 1 (2014) 57–70, https://doi.org/10.15377/2409-5818.2014.01.02.1.
[6] M. Alsehli, J.K. Choi, M. Aljuhan, A novel design for a solar powered multistage flash desalination, Sol. Energy 153 (2017) 348–359, https://doi.org/10.1016/j.solener.2017.05.082.
[7] A. Chorak, P. Palenzuela, D.C. Alarcón-Padilla, A. Ben Abdellah, Experimental characterization of a multi-effect distillation system coupled to a flat plate solar collector field: empirical correlations, Appl. Therm. Eng. 120 (2017) 298–313, https://doi.org/10.1016/j.applthermaleng.2017.03.115.
[8] N. Ghaffour, T.M. Missimer, G.L. Amy, Technical review and evaluation of the economics of water desalination: Current and future challenges for better water supply sustainability, Desalination 309 (2013) 197–207, https://doi.org/10.1016/j.desal.2012.10.015.
[9] E. Drioli, A. Ali, F. Macedonio, Membrane distillation: Recent developments and perspectives, Desalination 356 (2015) 56–84, https://doi.org/10.1016/j.desal.2014.10.028.
[10] B.B. Ashoor, S. Mansour, A. Giwa, V. Dufour, S.W. Hasan, Principles and applications of direct contact membrane distillation (DCMD): A comprehensive review, Desalination 398 (2016) 222–246, https://doi.org/10.1016/j.desal.2016.07.043.
[11] L. Eykens, I. Hitsov, K. De Sitter, C. Dotremont, L. Pinoy, I. Nopens, Van der Bruggen, Influence of membrane thickness and process conditions on direct contact membrane distillation at different salinities, J. Membr. Sci. 498 (2016) 353–364, https://doi.org/10.1016/j.memsci.2015.07.037.
[12] A. Deshmukh, C. Boo, V. Karanikola, S. Lin, A.P. Straub, T. Tong, D.M. Warsinger, M. Elimelech, Membrane distillation at the water-energy nexus: limits, opportunities, and challenges, Energy Environ. Sci. 11 (2018) 1177–1196, https://doi.org/10.1039/c8ee00291f.
[13] M. Khayet, Membranes and theoretical modeling of membrane distillation: A review, Adv. Colloid Interf. Sci. 164 (2011) 56–88, https://doi.org/10.1016/j.cis.2010.09.005.
[14] M.H. Sharqawy, J.H. Lienhard, S.M. Zubair, The thermophysical properties of seawater: A review of existing correlations and data, Desalin. Water Treat. 16 (2010) 354–380, https://doi.org/10.5004/dwt.2010.1079.
[15] M. Elimelech, W.A. Phillip, The Future of Seawater Desalination: Energy, Technology and the Environment, Science 333 (2011) 712–717, https://doi.org/10.1126/science.1200488.

[16] H.C. Duong, P. Cooper, B. Nelemans, T.Y. Cath, L.D. Nghiem, Evaluating energy consumption of air gap membrane distillation for seawater desalination at pilot scale level, Sep. Purif. Technol. 166 (2016) 55–62, https://doi.org/10.1016/j.seppur.2016.04.014.
[17] D. Winter, J. Koschikowski, D. Düver, P. Hertel, U. Beuscher, Evaluation of MD process performance: effect of backing structures and membrane properties under different operating conditions, Desalination 323 (2013) 120–133, https://doi.org/10.1016/j.desal.2013.04.007.
[18] S. Roy, M. Bhadra, S. Mitra, Enhanced desalination via functionalized carbon nanotube immobilized membrane in direct contact membrane distillation, Sep. Purif. Technol. 136 (2014) 58–65, https://doi.org/10.1016/j.seppur.2014.08.009.
[19] C. Yang, X.-M. Li, J. Gilron, D.-F. Kong, Y. Yin, Y. Oren, C. Linder, T. He, CF_4 plasma-modified superhydrophobic PVDF membranes for direct contact membrane distillation, J. Membr. Sci. 456 (2014) 155–161, https://doi.org/10.1016/j.memsci.2014.01.013.
[20] M. Essalhi, M. Khayet, Self-sustained webs of polyvinylidene fluoride electrospun nanofibers at different electrospinning times: 1. Desalination by direct contact membrane distillation, J. Membr. Sci. 433 (2013) 167–179, https://doi.org/10.1016/j.memsci.2013.01.023.
[21] Y. Liao, R. Wang, M. Tian, C. Qiu, A.G. Fane, Fabrication of polyvinylidene fluoride (PVDF) nanofiber membranes by electro-spinning for direct contact membrane distillation, J. Membr. Sci. 425–426 (2013) 30–39, https://doi.org/10.1016/j.memsci.2012.09.023.
[22] H. Ke, E. Feldman, P. Guzman, J. Cole, Q. Wei, B. Chu, A. Alkhudhiri, R. Alrasheed, B.S. Hsiao, Electrospun polystyrene nanofibrous membranes for direct contact membrane distillation, J. Membr. Sci. 515 (2016) 86–97, https://doi.org/10.1016/j.memsci.2016.05.052.
[23] K. Gethard, O. Sae-Khow, S. Mitra, Water desalination using carbon nanotube-enhanced membrane distillation, ACS Appl. Mater. Interfaces 3 (2011) 110–114, https://doi.org/10.1021/am100981s.
[24] W. Intrchom, S. Roy, S. Mitra, Functionalized carbon nanotube immobilized membrane for low temperature ammonia removal via membrane distillation, Sep. Purif. Technol. 235 (2020), 116188, https://doi.org/10.1016/j.seppur.2019.116188.
[25] X. Yang, R. Wang, L. Shi, A.G. Fane, M. Debowski, Performance improvement of PVDF hollow fiber-based membrane distillation process, J. Membr. Sci. 369 (2011) 437–447, https://doi.org/10.1016/j.memsci.2010.12.020.
[26] L. Eykens, K. De Sitter, C. Dotremont, L. Pinoy, B. Van der Bruggen, Membrane synthesis for membrane distillation: A review, Sep. Purif. Technol. 182 (2017) 36–51, https://doi.org/10.1016/j.seppur.2017.03.035.
[27] K.W. Lawson, M.S. Hall, D.R. Lloyd, Compaction of microporous membranes used in membrane distillation. I. Effects on gas permeability, J. Membr. Sci. 101 (1995) 99–108, https://doi.org/10.1016/0376-7388(94)00289-B.
[28] K.W. Lawson, D.R. Lloyd, Membrane distillation. II. Direct contact MD, J. Membr. Sci. 120 (1996) 123–133, https://doi.org/10.1016/0376-7388(96)00141-X.
[29] K.W. Lawson, D.R. Lloyd, Membrane distillation, J. Membr. Sci. 124 (1997) 1–25, https://doi.org/10.1016/S0376-7388(96)00236-0.
[30] A. Deshmukh, M. Elimelech, Understanding the impact of membrane properties and transport phenomena on the energetic performance of membrane distillation desalination, J. Membr. Sci. 539 (2017) 458–474, https://doi.org/10.1016/j.memsci.2017.05.017.
[31] A. Esfandiari, A.H. Monjezi, M. Rezakazemi, M. Younas, Computational fluid dynamics modeling of water desalination using low-energy continuous direct contact membrane distillation process, Appl. Thermal Eng. 163 (2019), 114391, https://doi.org/10.1016/j.applthermaleng.2019.114391.
[32] J. Phattaranawik, R. Jiraratananon, A.G. Fane, Effect of pore size distribution and air flux on mass transport in direct contact membrane distillation, J. Membr. Sci. 215 (2003) 75–85, https://doi.org/10.1016/S0376-7388(02)00603-8.
[33] Ó. Andrjesdóttir, C.L. Ong, M. Nabavi, S. Paredes, A.S.G. Khalil, B. Michel, D. Poulikakos, An experimentally optimized model for heat and mass transfer in direct contact membrane distillation, Int. J. Heat Mass Transf. 66 (2013) 855–867, https://doi.org/10.1016/j.ijheatmasstransfer.2013.07.051.
[34] G. Guan, R. Wang, F. Wicaksana, X. Yang, A.G. Fane, Analysis of membrane distillation crystallization system for high salinity brine treatment with zero discharge using aspen flowsheet simulation, Ind. Eng. Chem. Res. 51 (2012) 13405–13413, https://doi.org/10.1021/ie3002183.
[35] G. Guan, X. Yang, R. Wang, R. Field, A.G. Fane, Evaluation of hollow fiber-based direct contact and vacuum membrane distillation system using aspen process simulation, J. Membr. Sci. 464 (2014) 127–139, https://doi.org/10.1016/j.memsci.2014.03.054.
[36] A.S. Kim, Cylindrical cell model for direct contact membrane distillation (DCMD) of densely packed hollow fibers, J. Membr. Sci. 455 (2014) 168–186, https://doi.org/10.1016/j.memsci.2013.12.067.
[37] K.M. Lisboa, J.R.B. de Souza, C.P. Naveira-Cotta, R.M. Cotta, Heat and mass transfer in hollow-fiber modules for direct contact membrane distillation: Integral transforms solution and parametric analysis, Int. Commun. Heat Mass Transf. 109 (2019), 104373, https://doi.org/10.1016/j.icheatmasstransfer.2019.104373.
[38] L. Li, K.K. Sirkar, Influence of microporous membrane properties on the desalination performance in direct contact membrane distillation, J. Membr. Sci. 513 (2016) 280–293, https://doi.org/10.1016/j.memsci.2016.04.015.
[39] L. Eykens, K. De Sitter, C. Dotremont, L. Pinoy, B. Van der Bruggen, How to optimize the membrane properties for membrane distillation: A review, Ind. Eng. Chem. Res. 55 (2016) 9333–9343, https://doi.org/10.1021/acs.iecr.6b02226.
[40] R. Ullah, M. Khraisheh, R.J. Esteves, J.T. McLeskey Jr., M. AlGhouti, M. Gad-el-Hak, H.V. Tafreshi, Energy efficiency of direct contact membrane distillation, Desalination 433 (2018) 56–67, https://doi.org/10.1016/j.desal.2018.01.025.
[41] S. Whitaker, Flow in porous media I: A theoretical derivation of Darcy's law, Transp. Porous Med. 1 (1986) 3–25, https://doi.org/10.1007/BF01036523.
[42] D.A. Nield, A. Bejan, Convection in Porous Media, 5th ed., Springer, Cham, Switzerland, 2017.
[43] S.N. Singh, Heat transfer by laminar flow in a cylindrical tube, Appl. Sci. Res. 7 (1958) 325–340, https://doi.org/10.1007/BF03184993.
[44] K.M. Lisboa, "Analysis of the membrane effects on the energy efficiency of water desalination in a Direct Contact Membrane Distillation (DCMD) system with heat recovery, Mendeley Data 2 (2020), https://doi.org/10.17632/z7y3dt35rc.2.
[45] M. Gryta, M. Tomaszewska, Heat transport in membrane distillation process, J. Membr. Sci. 144 (1998) 211–222, https://doi.org/10.1016/S0376-7388(98)00050-7.
[46] V. Gnielinski, New equations for heat and mass transfer in turbulent pipe and channel flow, Int. Chem. Eng. 16 (1976) 359–368.
[47] R.W. Field, H.Y. Wu, J.J. Wu, Multiscale modeling of membrane distillation: Some theoretical considerations, Ind. Eng. Chem. Res. 52 (2013) 8822–8828, https://doi.org/10.1021/ie302363e.
[48] R.W. Schofield, A.G. Fane, C.J.D. Fell, R. Macoun, Factors affecting flux in membrane distillation, Desalination 77 (1990) 279–294, https://doi.org/10.1016/0011-9164(90)85030-E.
[49] D.R. Lide, W.M. Haynes, Handbook of Chemistry and Physics, 90th ed., CRC Press, Boca Raton, FL, 2010.
[50] Wolfram, S., Wolfram Research Inc., Mathematica v.11, 2018.
[51] B.S. Sparrow, Empirical equations for the thermodynamic properties of aqueous sodium chloride, Desalination 159 (2003) 161–170, https://doi.org/10.1016/S0011-9164(03)90068-3.
[52] Z. Wang, T. Horseman, A.P. Straub, N.Y. Yip, D. Li, M. Elimelech, S. Lin, Pathways and challenges for efficient solar-thermal desalination, Sci. Adv. 5 (2019) eaax0763, https://doi.org/10.1126/sciadv.aax0763.
[53] S. Kakaç, H. Liu, Heat Exchangers: Selection, Rating, and Thermal Design, 2nd ed., CRC Press, Boca Raton, FL, 2002.
[54] G. Neale, Degrees of anisotropy for fluid flow and diffusion (electrical conduction) through anisotropic porous media, AIChE Journal 23 (1977) 56–62, https://doi.org/10.1002/aic.690230110.
[55] K.Y. Wang, T.-S. Chung, M. Gryta, Hydrophobic PVDF hollow fiber membranes with narrow pore size distribution and ultra-thin skin for the fresh water production through membrane distillation, Chem. Eng. Sci. 63 (2008) 2587–2594, https://doi.org/10.1016/j.ces.2008.02.020.
[56] J. Devore, N. Farnum, J. Doi, Applied Statistics for Engineers and Scientists, 3rd ed., Cengage Learning, Stamford, CT, 2014.
[57] A. Alabastri, P.D. Dongare, O. Neumann, J. Metz, I. Adebiyi, P. Nordlander, N. J. Halas, Resonant energy transfer enhances solar thermal desalination, Energy Environ. Sci. 13 (2020) 968–976, https://doi.org/10.1039/C9EE03256H.